Accelerated Structure-Aware Sparse Bayesian Learning for 3D Electrical Impedance Tomography

Accelerated Structure-Aware Sparse Bayesian Learning for 3D Electrical Impedance Tomography

Shengheng Liu, *Member, IEEE*, Hancong Wu, *Student Member, IEEE*, Yongming Huang, *Senior Member, IEEE*, Yunjie Yang, *Member, IEEE*, and Jiabin Jia, *Member, IEEE*

***Abstract*—In this work, we consider the reconstruction of three-dimensional (3D) conductivity distribution using electrical impedance tomography (EIT) technique. A high-resolution and efficient algorithm is developed to solve the EIT inverse problem. The presented algorithm is extended upon a recently proposed novel EIT reconstruction approach based on structure-aware sparse Bayesian learning (SA-SBL). The correlation between proximal layers in the 3D geometry are incorporated into the structure prior to improve the reconstruction accuracy. In addition, an efficient approach based on approximate message passing is developed to accelerate the large-scale 3D learning process. To validate the algorithm, numerical experiments using real recorded data are conducted. The visual and quantitative-metric comparisons show that the proposed method outperforms the existing methods in terms of reconstruction accuracy and computational complexity in all test cases. The SA-SBL based reconstruction approach can preserve the 3D structure of medical volume, reduce the systematic artifacts, and improve the computational efficiency.**

***Index Terms*—Inverse problem, electrical impedance tomography (EIT), sparse Bayesian learning (SBL), image reconstruction, three-dimensional geometry.**

I. Introduction

NON-DESTRUCTIVE examination and visualization of the internal industrial/biological process within a certain object is frequently and increasingly demanded in practice. Compared with other popular imaging modalities, such as ultrasound [1] and computed tomography (CT) [2], electrical impedance tomography (EIT) possesses the merits of higher temporal resolution, lower cost, wider applicability, and etc. However, EIT reconstruction is inherently instable and suffers from the fundamental ill-posedness of the underlying inverse problem. The susceptibility of EIT solution to the measurement, numerical, and modeling errors necessitates regularization, and numerous such methods has been developed over the years. While the majority of EIT reconstruction algorithms has been designed for two-dimensional (2D) geometries (cf. literature review in [3]), a single cross-sectional slice of the volume can only reveal partial information of the realistic three-dimensional (3D) objects and thus limit the capacity of EIT. On the other hand, EIT is intrinsically a 3D problem [4], for it is well known that the path of the electric currents spread all over the 3D domain. As such, off-plane conductivity changes generally affect the solutions of the electrode plane and create considerable distortions in the resulting 2D images [5]. These severe limitations to 2D EIT thus encourage the development of 3D reconstruction. It is worth mentioning that, most 2D reconstruction methods are also applicable in 3D situations with minor modifications, and methods for both situations have been occasionally discussed together indiscriminately.

Fully 3D EIT has been investigated since 1980s. Calderón's pioneer work [6] outlined a linearized method for the reconstruction of the multidimensional conductivity in a bounded domain, which laid the mathematical foundation for 3D EIT. Thenceforth many algorithms have been developed, including double constraint iterative algorithm [7], variants of Newton's One-Step Error Reconstruction (NOSER) [8]–[10], Markov chain Monte Carlo (MCMC) based Bayesian approach [11], and etc. Apart from the linear approaches, various nonlinear solvers have also been produced. However, these were either facilitating a Newton-type strategy, which is highly computational intensive for large-scale problems, or employing the Krylov-subspace approach, which suffers from poor convergence rate [12]. In [13], a fully iterative regularized Gauss-Newton method was applied to 3D tank data adopting the complete electrode model (CEM) [14], which is the most accurate model for real-world EIT. In this paper, we also work exclusively with CEM. Readers are also referred to important articles [4], [15], where various commonly used conventional 3D reconstruction algorithms, such as regularised Gauss-Newton and conjugate-gradient based algorithms, were evaluated using simulated and real experimental data. The results of the study suggested that 3D EIT algorithms do have value and require further development.

Studies of 3D EIT in the early period was restrained by the prohibitive consumption of computing and storage resources, which partly explains why 2D assumptions were constantly made. Later, advances in electronic devices made the true 3D EIT reconstruction technically more feasible. The release of software EIDORS [16] marked another significant milestone in the progress of 3D EIT. Since then, other more

Manuscript received August 16, 2018; revised December 12, 2018 and January 3, 2019; accepted January 22, 2019. Date of publication XXX XX, XXXX; date of current version XXX XX, XXXX. This work was supported in part by the UK's Engineering and Physical Sciences Research Council (EPSRC) under Grant No. EP/P006833/1. Startup funding from the Southeast University is also acknowledged for support of this work. Paper no. TII-18-2139.R2. (Corresponding author: Y. Huang.)

S. Liu and Y. Huang are with the School of Information Science and Engineering, Southeast University, Nanjing 210096, China (e-mail: s.liu@seu.edu.cn; huangym@seu.edu.cn).

H. Wu, Y. Yang, and J. Jia are with the Agile Tomography Group, Institute for Digital Communications, School of Engineering, The University of Edinburgh, Edinburgh EH9 3JL, UK (e-mail: jiabin.jia@ed.ac.uk).

Color versions of one or more of the figures in this paper are available online at http://ieeexplore.ieee.org.

Digital Object Identifier 10.1109/TII.2019.XXXXXXX

recent approaches, including topology optimization approach [17], direct reconstruction using scattering transforms [18], iterative soft shrinkage algorithm [19], Bayesian approach with edge-preferring priors [20], TV regularization [21], nonlinear approach [22], and 3D-Laplacian and sparsity joint regularization algorithm [23] have been proposed. Despite considerable effort for nearly three decades, existing 3D EIT reconstruction algorithms fail to efficiently and reliably produce images with sufficiently high spatial resolution. Moreover, many algorithms (perhaps the majority) are *ad hoc* and require tweaking of parameters that prevents repeatability in experimentation. Specifically in the field of bioengineering, 3D EIT has yet to make the transition from theoretical studies to practical use.

The quality of reconstructed images and the efficiency of the reconstruction process are two major concerns for 3D EIT. One most recent publication [3] has proposed a novel structure-aware sparse Bayesian learning (SA-SBL) algorithm for 2D EIT reconstruction, with which an enhanced spatial resolution was achieved. The underlying structural dependency of signals can be readily incorporated within the Bayesian framework. Several challenging problems in industrial applications have been successfully tackled on this account. For example, adaptive resource management in intelligent wireless sensor networks can be realized by exploring the temporal structure among observations in a dynamic Bayesian network [24]; glutamic acid fermentation process can also be predicted using a Bayesian fuzzy system, which involves structure identification and parameter estimation of each fuzzy rule therein [25]. This paper considers 3D geometry and expands upon [3] and its follow-up studies [27], [28] in several important ways. The presented 3D EIT reconstruction algorithm could potentially be useful for designing real-time industrial/bioengineering sensor systems that yields EIT imaging of practical significance. The main contributions of this papers are:

- First, the structure prior is redesigned to take into account the correlation between proximal layers in the 3D geometry, which yields an improved recovery performance and algorithm robustness;
- Another important contribution of the present work is that, to achieve efficient computation, an approximate message passing (AMP) accelerated expectation maximization (EM) technique is proposed to infer the maximum *a posteriori* (MAP) estimates.
- In addition, an experiment is also designed to investigate the fluid flow using EIT modality in a 3D geometry, where accurate revivification is achieved. This suggests feasibility of using EIT to monitor similar processes in industrial and bioengineering applications, which is of great practical significance.

The remainder of this paper is structured as follows: In the Method section we first present the SA-SBL-based 3D EIT reconstruction algorithm. Then, in Section III we describe and discuss the experiments performed to validate our approach. The paper is concluded in Section IV.

II. Method

In this work, we consider an inverse problem of linearized time-difference EIT of the form [3]

$$\mathbf{v} = \mathbf{J}\boldsymbol{\sigma} + \mathbf{n}, \tag{1}$$

where

- $\mathbf{v} \in \mathbb{R}^{M\times 1}$ represents the time-difference vector of the voltage measurements, and M denotes the length of the measurement vector.
- $\mathbf{J} \in \mathbb{R}^{M\times N}$ is the sensitivity matrix, and N denotes the number of simplices in the 3D domain.
- $\boldsymbol{\sigma} \in \mathbb{R}^{N\times 1}$ represents the 3D time-difference conductivity distribution to be reconstructed.
- $\mathbf{n} \in \mathbb{R}^{M\times 1}$ denotes the measurement noise vector, which is assumed to be Gaussian, i.e., $\mathbf{n} \sim \mathcal{N}(\mathbf{0}, \gamma_0\mathbf{I})$.

Similar to [3], [26], we let $g = N - h + 1$ be the total number of groups. For $\forall i = 1, 2, \ldots, g$, $\boldsymbol{\sigma}$ is factorized as (2) to facilitate the utilization of SA-SBL framework. Substituting (2) into (1), we then obtain the following stretched linear model

$$\mathbf{v} = \boldsymbol{\Phi}\mathbf{x} + \mathbf{n}, \tag{3}$$

where $\boldsymbol{\Phi} \triangleq \mathbf{J}\boldsymbol{\Psi} \in \mathbb{R}^{M\times gh}$. We follow the standard Bayesian formulation and assume that both of the priors of the weights $\mathbf{x}$ and the noise vector $\mathbf{n}$ follow parameterized Gaussian distributions, i.e., $\mathbf{x} \sim \mathcal{N}(\mathbf{0}, \boldsymbol{\Sigma}_0)$, $\mathbf{n} \sim \mathcal{N}(\mathbf{0}, \gamma_0\mathbf{I})$, where the stretched covariance matrix is expressed as $\boldsymbol{\Sigma}_0 = \mathrm{diag}(\gamma_i\mathbf{B}_i) \in \mathbb{R}^{gh\times gh}$. The positive definite matrix $\mathbf{B}_i$ determines the correlated structure within the i-th block of $\mathbf{x}$. Due to the mechanism of automatic relevance determination, most γ_i's tend to become zero during the learning process, thus promoting the group-level sparsity.

The posterior distribution for $\mathbf{x}$ can be expressed analytically as $\mathbf{x}|\mathbf{v} \sim \mathcal{N}(\boldsymbol{\mu}_x, \boldsymbol{\Sigma}_x)$ with mean and covariance matrix

$$\boldsymbol{\mu}_x = \boldsymbol{\Sigma}_0\boldsymbol{\Phi}^\top\boldsymbol{\Gamma}^{-1}\mathbf{v} \in \mathbb{R}^{gh\times 1}, \tag{4}$$

$$\boldsymbol{\Sigma}_x = \boldsymbol{\Sigma}_0 - \boldsymbol{\Sigma}_0\boldsymbol{\Phi}^\top\boldsymbol{\Gamma}^{-1}\boldsymbol{\Phi}\boldsymbol{\Sigma}_0 \in \mathbb{R}^{gh\times gh}, \tag{5}$$

$$\begin{aligned}\boldsymbol{\sigma} &\triangleq \boldsymbol{\Psi}_{N\times gh}\mathbf{x}_{gh\times 1} \\ &\triangleq \begin{bmatrix} \begin{bmatrix} \mathbf{1}_{h\times h} \\ \mathbf{0}_{(N-h)\times h} \end{bmatrix} & \cdots & \begin{bmatrix} \mathbf{0}_{(i-1)\times h} \\ \mathbf{1}_{h\times h} \\ \mathbf{0}_{(N-i-h+1)\times h} \end{bmatrix} & \cdots & \begin{bmatrix} \mathbf{0}_{(N-h)\times h} \\ \mathbf{1}_{h\times h} \end{bmatrix} \end{bmatrix} \cdot \begin{bmatrix} \begin{bmatrix} x_1 & \cdots & x_h \end{bmatrix}^\top \\ \vdots \\ \begin{bmatrix} x_i & \cdots & x_{i+h-1} \end{bmatrix}^\top \\ \vdots \\ \begin{bmatrix} x_g & \cdots & x_N \end{bmatrix}^\top \end{bmatrix}\end{aligned} \tag{2}$$

where

$$\mathbf{\Gamma} \triangleq \gamma_0 \mathbf{I} + \mathbf{\Phi} \mathbf{\Sigma}_0 \mathbf{\Phi}^\top \in \mathbb{R}^{M \times M}. \tag{6}$$

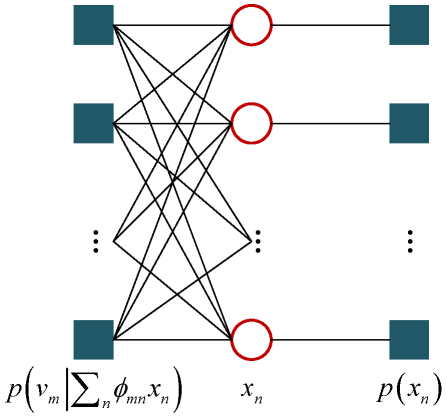

Fig. 1. AMP factor graph representation.

The first step in the SA-SBL-based EIT reconstruction [3] is to update the hyperparameters $\Theta \triangleq \{\gamma_0, \{\gamma_i, \mathbf{B}_i\}_{i=1}^g\}$. This is achieved by employing the expectation-maximization (EM) method to minimize the cost function $\mathcal{L}(\Theta) = \log|\mathbf{\Gamma}| + \mathbf{v}^\top \mathbf{\Gamma}^{-1} \mathbf{v}$. Subsequently, the MAP probability estimate $\widehat{\mathbf{x}}$ is obtained directly from the posterior mean $\boldsymbol{\mu}_x$. Up to this point, one would naturally assume that the 2D EIT reconstruction algorithm in [3] can be directly applied to the 3D scenario, as the underlying mathematical problem intrinsically remains unchanged. However, the computational complexity of the previously proposed EM-based SA-SBL algorithm is dominated by the expectation step (E-step), i.e., (4) and (6), which respectively involves $O(MN^2)$ and $O(N^3)$ multiplications per iteration. In this context, the large-scale weight length N in the 3D model makes the inversion via SA-SBL computationally intractable.

Recently, the AMP methods [29]–[31] have received growing attention due to their low computational complexity, fast convergence, and close-to-Bayes-optimal estimation. We illustrate the AMP framework in Fig. 1, where blue squares and red circles represent probability density function (pdf) factors and random variables, respectively. Gaussian approximated belief propagation is performed. Concretely, the posterior pdf is first factorized into a product of simpler pdfs. Then, the locally computed messages associated with the unknown variables are passed around the factor graph until agreement on a common set of beliefs is arrived. By assuming a large and dense measurement matrix and exploiting similarity among the messages, central limit theorem and Taylor series expansion are adopted to approximate the inference.

In this work, AMP is applied to simplify the computational expensive E-step of SA-SBL-based 3D EIT reconstruction. We summarize the algorithm flow in **Algorithm 1**, where $\otimes$ and $\oslash$ respectively denote Hadamard product and element-wise division. It can be readily observed from **Algorithm 1** that, $\mathbf{\Phi}$, $\mathbf{S}$, and their transposes related vectorized multiplications constitute the majority of the overall computation load. As such, the E-step is implemented by a first-order algorithm with a computational complexity of $O(MN)$ per iteration.

It should be noted that, as Gaussian prior is imposed on the weights $\mathbf{x}$, the algorithm is parameterized by the following two scalar estimation functions:

$$f_s(\mathbf{p}, \boldsymbol{\alpha}_p) = (\mathbf{p} \oslash \boldsymbol{\alpha}_p - \mathbf{v}) \oslash (\gamma_0 + 1 \oslash \boldsymbol{\alpha}_p), \tag{7}$$

$$f_x(\mathbf{r}, \boldsymbol{\tau}_r) = (\boldsymbol{\gamma} \otimes \mathbf{r}) \oslash (\boldsymbol{\gamma} + \boldsymbol{\tau}_r). \tag{8}$$

Algorithm 1: AMP-based E-step approximation.

Input : $\mathbf{\Phi}$, $\theta_s, \theta_x \in (0, 1]$, ϵ_{AMP}.
Initialize : Set $\mathbf{S} = \mathbf{\Phi} \otimes \mathbf{\Phi}$, $\mathbf{s} = \mathbf{0}$, $\boldsymbol{\mu}_x = \mathbf{0}$, $\boldsymbol{\tau}_x \succ \mathbf{0}$, $\epsilon = 1$.
Iterations:
1 **while** $\epsilon > \epsilon_{\text{AMP}}$ **do**
2 $\quad \boldsymbol{\alpha}_p = \mathbf{1} \oslash (\mathbf{S}\boldsymbol{\tau}_x)$,
3 $\quad \mathbf{p} = \mathbf{s} + \boldsymbol{\alpha}_p \otimes \mathbf{\Phi}\boldsymbol{\mu}_x$,
4 $\quad \boldsymbol{\alpha}_s = \boldsymbol{\alpha}_p \otimes \frac{\partial}{\partial \mathbf{p}} f_s(\mathbf{p}, \boldsymbol{\alpha}_p)$,
5 $\quad \mathbf{s} = (1 - \theta_s)\mathbf{s} + \theta_s f_s(\mathbf{p}, \boldsymbol{\alpha}_p)$,
6 $\quad \boldsymbol{\tau}_r = \mathbf{1} \oslash (\mathbf{S}^\top \boldsymbol{\alpha}_s)$,
7 $\quad \mathbf{r} = \boldsymbol{\mu}_x + \boldsymbol{\tau}_r \otimes \mathbf{\Phi}^\top \mathbf{s}$,
8 $\quad \boldsymbol{\tau}_x = \boldsymbol{\tau}_r \otimes \frac{\partial}{\partial \mathbf{r}} f_x(\mathbf{r}, \boldsymbol{\tau}_r)$,
9 $\quad \boldsymbol{\mu}_x = (1 - \theta_x)\boldsymbol{\mu}_x + \theta_x f_x(\mathbf{r}, \boldsymbol{\tau}_r)$,
10 $\quad \epsilon = \|\boldsymbol{\mu}_x^{\text{new}} - \boldsymbol{\mu}_x\|_2 / \|\boldsymbol{\mu}_x^{\text{new}}\|_2$.
11 **end**
Output : $\widehat{\boldsymbol{\mu}}_x$, $\widehat{\boldsymbol{\tau}}_x$

Remarks 1: The Onsager correction term in step 7 is the key to the increased accuracy and computational efficiency of AMP methods, for it decouples prediction errors across iterations and ensure that r is an i.i.d.-Gaussian corrupted version of the true x. In addition, to prevent divergence caused by the ill-conditioned measurement matrix with strongly correlated columns, damping mechanism is introduced in step 5 and 9.

Once the parameters $\widehat{\boldsymbol{\mu}}_x$ and $\widehat{\boldsymbol{\tau}}_x$ for the expected distribution are obtained, the algorithm continues to infer the hyperparameters $\Theta \triangleq \{\gamma_0, \{\gamma_i, \mathbf{B}_i\}_{i=1}^g\}$ through the maximization iterations as we did in [3]. Note that, the learning rules for these hyperparameters are slightly different from our previous work in [3]. Concretely, the regularized correlation structure matrix $\mathbf{B}_i$ is updated as

$$\mathbf{B}_i = \text{Toeplitz}\left(\left[r_i^0, r_i^1, \ldots, r_i^{h-1}\right]\right), \tag{9}$$

with

$$r_i = \text{sign}(\tilde{r}_i) \cdot \min\left\{|\tilde{r}_i|, 0.99\right\}, \tag{10}$$

$$\tilde{r}_i = \overline{\text{diag}(\widetilde{\mathbf{B}}_i, 1)} \Big/ \overline{\text{diag}(\widetilde{\mathbf{B}}_i)}. \tag{11}$$

$$\widetilde{\mathbf{B}}_i^{\text{new}} = \widetilde{\mathbf{B}}_i + \frac{1}{\gamma_i}\left(\text{diag}(\widehat{\boldsymbol{\tau}}_x^i) + \widehat{\boldsymbol{\mu}}_x^i \left(\widehat{\boldsymbol{\mu}}_x^i\right)^\top\right), \tag{12}$$

where the superscript i denotes the $((i-1)h+1 : ih)$-th entries of the corresponding vectors.

To better exploit the 3D structure correlation so as to enhance the reconstruction accuracy, a 3D pattern coupling parameter $\beta \in [0, 1]$ is introduced to the updating formula of γ_i to capture the dependency between the simplex under investigation and its proximal 6 simplexes (see Fig. 2). As

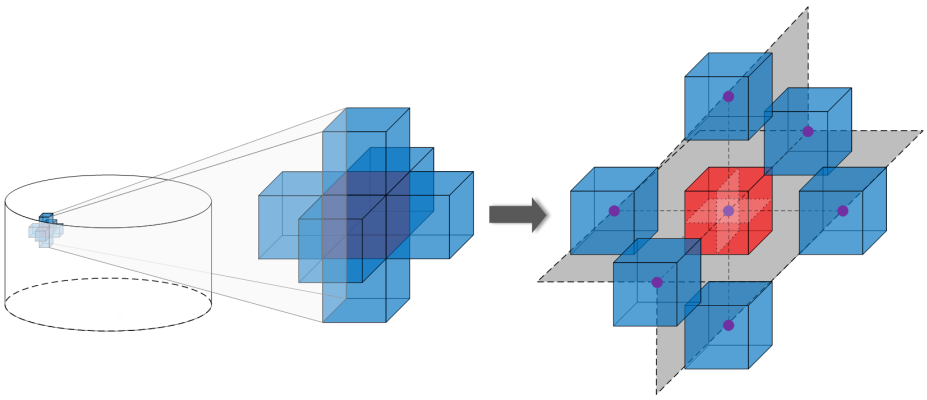

Fig. 2. Illustration of the structure in the conductivity distribution $\boldsymbol{\sigma}$.

such, an updated γ_i in each iteration can be expressed as follows:

$$\gamma_i^{\text{new}} = (\gamma_i + \beta \sum_{d=1}^{6} \tilde{\gamma}_{i,d}) \cdot \frac{\text{tr}\left(\mathbf{B}_i^{-1}\left(\text{diag}(\widehat{\boldsymbol{\tau}}_x^i) + \widehat{\boldsymbol{\mu}}_x^i \left(\widehat{\boldsymbol{\mu}}_x^i\right)^\top\right)\right)}{h}, \tag{13}$$

Likewise, hyperparameter γ_0 is learned by

$$\gamma_0^{\text{new}} = \frac{\|\mathbf{v} - \boldsymbol{\Phi}\widehat{\boldsymbol{\mu}}_x\|_2^2 + \sum_{i=1}^{g} \text{tr}\left(\text{diag}(\widehat{\boldsymbol{\tau}}_x^i)(\boldsymbol{\Phi}_i)^\top \boldsymbol{\Phi}_i\right)}{M}. \tag{14}$$

A pseudo-code implementation of the overall algorithm for 3D EIT reconstruction is presented in **Algorithm 2**. As stated in [3], h and β are two tuning-free parameters, and we set $h = 4$ and $\beta = 0.25$ in the following discussion. ϵ_{AMP} in **Algorithm 1** and $\vartheta_{\max}$ in **Algorithm 2** are both selected according to the precision requirement and computational resource.

Remarks 2: The initial guess of the parameters in **Algorithm 2** such as γ_0 is empirically selected by extensive numerical trials, which generally leads to a faster convergence. It has little impact on the algorithm performance since these parameters will be automatically learned afterwards.

Algorithm 2: SA-SBL-based 3D EIT reconstruction.

Input : $\mathbf{v}$, $\mathbf{J}$, h, β, $\vartheta_{\max}$

Initialize : Set $\vartheta = 0$, $\gamma_i = \mathbf{1}_{g\times 1}$,

$$\gamma_0 = 0.01 \times \sqrt{\frac{1}{N-1}\sum_{i=1}^{N} |v_i - \bar{\mathbf{v}}|^2},$$

$$\mathbf{B}_i = \text{Toeplitz}([0.9^0, \ldots, 0.9^{h-1}]).$$

Iterations:

while $\vartheta \leq \vartheta_{\max}$ **do**
- Execute approximated E-step in **Algorithm 1**;
- Update γ_i using (13);
- Update γ_0 using (14);
- Update $\mathbf{B}_i$ using (12)–(11);
- $\vartheta = \vartheta + 1$.

end

Output : $\widehat{\boldsymbol{\sigma}} = \boldsymbol{\Psi}\widehat{\boldsymbol{\mu}}_x$

III. Experiment Results and Discussions

In this section, the proposed 3D EIT reconstruction algorithm is evaluated with real-collected data. We consider two different experimental scenarios, viz., 3D cell pellet imaging and 3D Process Tomography of solution diffusion.

In the first experimental evaluation, we reconstruct the 3D EIT image from the dataset that has been utilized in [23]. The voltage measurement under test was recorded using a planar 3D miniature EIT sensor designed for cell imaging. Fast and

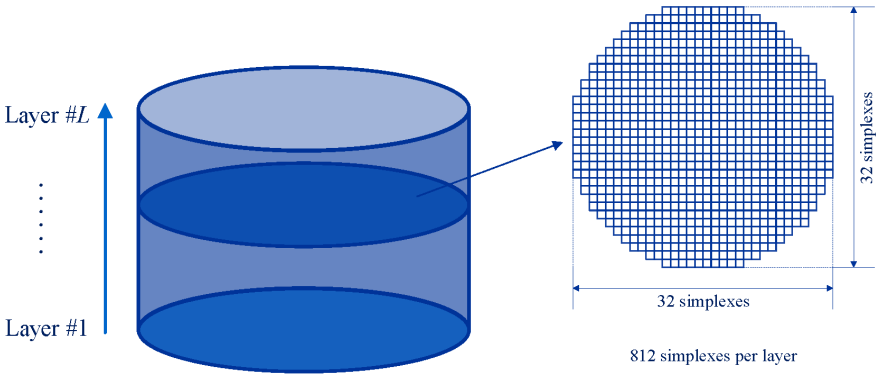

Fig. 3. 3D inverse mesh.

high-spatial-resolution reconstruction algorithm is particularly desirable in the scenario of continuous monitoring of cell culture process. Such task is considered challenging because of the small size of the sensor/subject and the high conductivity of the culture medium [23]. In the second experiment, the jet saline flow experiment in the Section IV-B of [3] is further extended to a 3D geometry. We still acquire the EIT measurements with the same cylindrical vessel senor used in [3], but two electrode planes are enabled to collect the voltage data at this time.

The 3D inverse finite element method (FEM) mesh in both reconstruction processes is illustrated in Fig. 3. While each layer in the FEM meshes for both experiments consists of 821 square simplices, the numbers of layers L in the two FEM meshes are different. The former FEM mesh in Section III-A has 12 layers, and the latter in Section III-B has 40 layers. Consequently, the numbers of 3D simplices N for these two experiments are 9744 and 32480, respectively.

A. 3D Cell Pellet Imaging

In the cell pellet imaging experiment, phosphate buffered saline with a conductivity of $1.9\ \mathrm{S/m}$ and height of $3\ \mathrm{mm}$ is used as cell culture medium. The internal diameter of the sensor is $15\ \mathrm{mm}$. The frequency of current excitation is $10\ \mathrm{KHz}$, and the amplitude of current is approximately $1.5\ \mathrm{mA}$ peak to peak. A triangular high-density breast cancer cell pellet is used as the experimental subject to be measured, which is shown in Fig. 4. The length of the trilateral is around $4.2\ \mathrm{mm}$, $3.6\ \mathrm{mm}$, and $4.5\ \mathrm{mm}$, respectively.

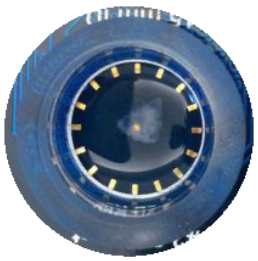

Fig. 4. Truth of the triangular cell pellet to be measured. (Adapted from Fig. 15(c) of [23]. Reuse with the permission from IEEE and the authors.)

A comparison is drawn in Table I, which shows the 3D EIT reconstruction results of the phantom using the conventional Bayesian algorithm [32] and the proposed SA-SBL based algorithm, respectively. Note that in Table I the two images in the first row of each table box are the 3D isosurface generated from the resulting volumetric data and the corresponding lateral view, respectively. The isovalue is specified as 40% of the maximum conductivity value. White grids are added into the slice plots to allow for a more precise assessment of the reconstruction. The readers are referred to the previous related work in [23] for a comparison of reconstructed results using other deterministic algorithms.

Because the subject to be imaged is a compound of cell pellet and agarose gel with an irregular shape, and part of the compound is transparent in the field of vision, we are unable to give a precise position of the inclusion. Since neither do we have an exact truth of the conductivity distribution under investigation, a quantitative evaluation of the advantage of the proposed algorithm in terms of spatial resolution and reconstruction accuracy cannot be provided. But it is important to note that, the presented algorithm in this paper is essentially a 3D and computationally efficient extension of the SA-SBL-based EIT reconstruction algorithm in [3] with the aid of AMP-based EM iteration. The effectiveness of the SA-SBL-based algorithm in comparison with other state-of-the-art approaches has been demonstrated via sufficient synthetic data simulations in COMSOL environment. On the other hand, it has been proved with extensive numerical studies in [30] that, AMP technique is able to yield nearly minimum mean-squared error recovery. In the light of the above facts, it is unnecessary to repeat the COMSOL-based numerical verification.

As indicated in Fig. 4, the utilized dataset is essentially a pseudo-3D measurement collected from a single electrode ring. Additionally, the EIT senor and subject to be detected are both in a extremely small size. Therefore, it is reasonable to anticipate a poor reconstruction result by using conventional methods. Nevertheless, the advantage of the proposed SA-SBL based algorithm in terms of algorithm performance can be visually observed from Table I. More specifically, the proposed algorithm is able to render a clear and accurate 3D image of the triangular cell pellet, whereas with the conventional Bayesian algorithm, conspicuous errors in the reconstructed shape/height of the phantom and undesired artifacts especially in the near-boundary region can be seen. 3D structural priors intuitively introduce additional constraints to stabilize the recovered images and, thus, make them more robust to interference and noise.

B. 3D Process Tomography of Jet Flow

EIT and the related electrical capacitance tomography (ECT) [33] are emerging techniques for imaging the flow and mixing of fluids in various industrial and biomedical applications. In this work, another experiment is designed to demonstrate the feasibility of fast and accurate 3D EIT-based process monitoring of fluid flow. Jet flows are simulated in the experiment since they are amongst the most frequently encountered flow types.

The vessel senor adopts an alternate mode to acquire the measurements for 3D imaging, i.e., the voltmeter readings in each plane are alternately drawn by switching the channels back and forth. The inner diameter of the cylindrical vessel is $287\ \mathrm{mm}$, and the height of the background substance is $200\ \mathrm{mm}$. The current excitation frequency and the injected current amplitude remain the same as [3], which are respectively $10\ \mathrm{kHz}$ and $15.17\ \mathrm{mA}$. The frame collection rate is set to $62.5\ \mathrm{fps}$. We select one frame from every 8 frames between the 460-th and the 516-th frame. The conductivities of the red jet ink and the background saline are set to $0.8\ \mathrm{S/m}$ and $0.25\ \mathrm{S/m}$ respectively. The successive video snapshots and the reconstructed conductivity distributions by using the proposed algorithm for the selected frames are shown in Table II. To create a legible visualization, we first compare the absolute value of each entry with the threshold in each frame, which

TABLE I
3D EIT RECONSTRUCTION RESULTS OF THE TRIANGULAR CELL PELLET.

Conventional Bayesian method	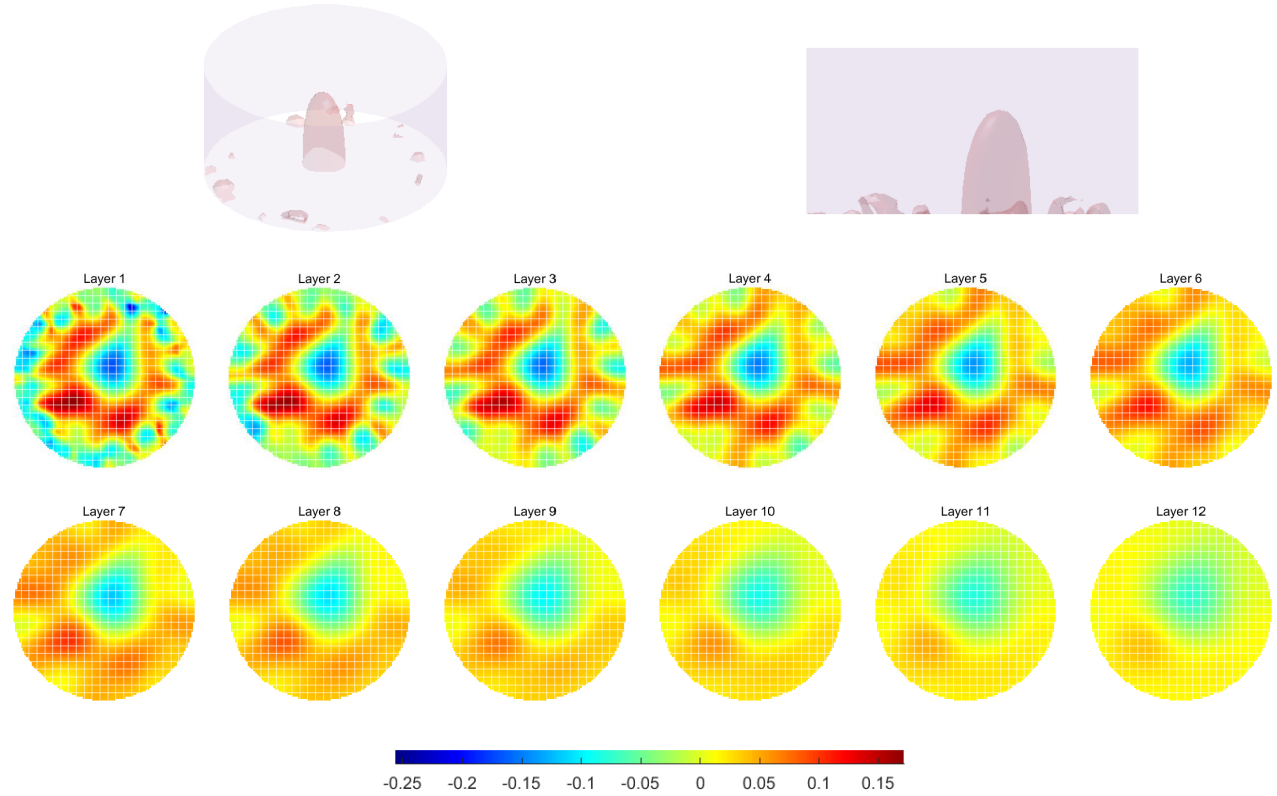
Proposed method	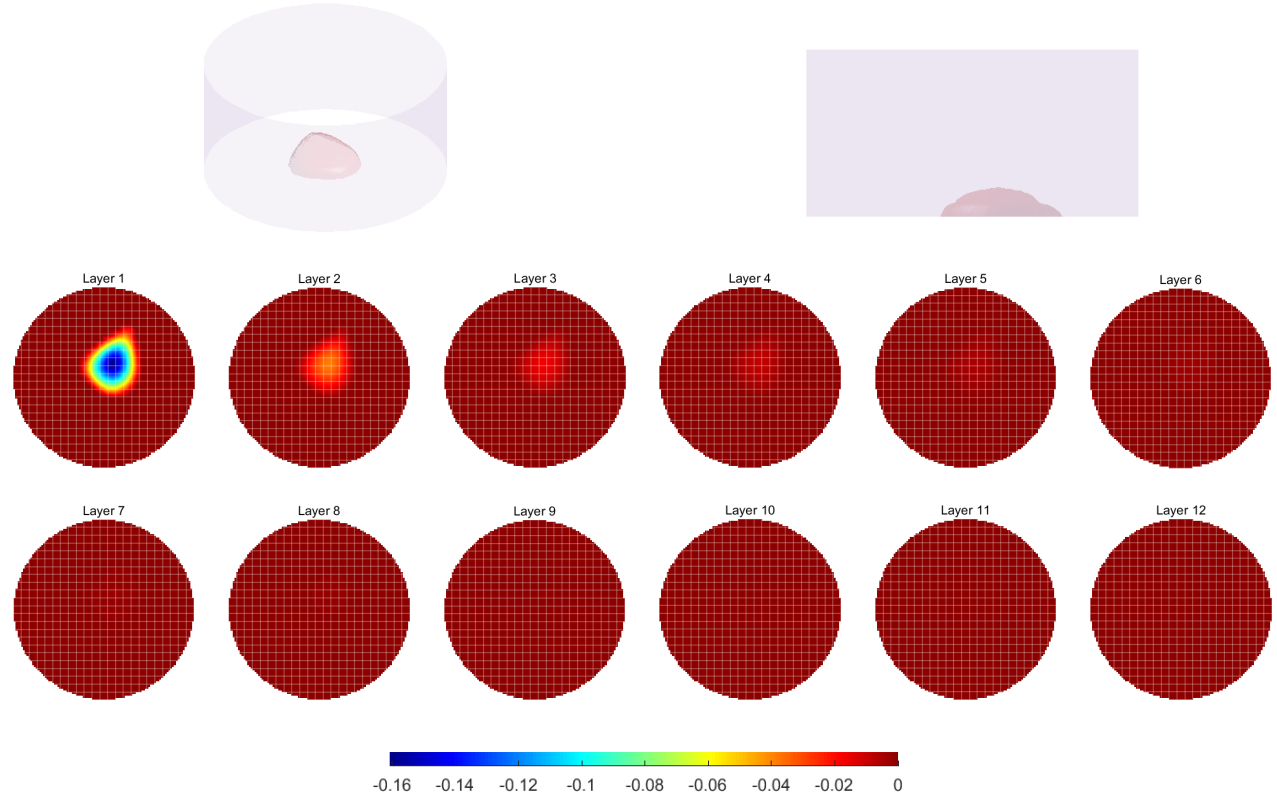

is set to 40% of the maximum absolute value in the frame. We then discard the conductivity values below the threshold and draw slices through the resulting EIT volumetric data. As such, only significant values induced by the jet flow are preserved and visualized in the 3D slices in Table II, so that the occlusions caused by the background and noise are removed. It can be observed from Table II that the estimates are in a good agreement with their corresponding video snapshots. Very few peripheral artifacts exist, and the entire injection process of the jet flow is accurately reconstructed.

Remarks 3: Note that the threshold 40% adopted in producing Table II is empirically selected for illustrative purpose. The use of a fixed percentage cut-off from the maximum value may lead to incorrect EIT result if there are no inclusions inside the sensor. In this situation, background fluctuations may not be filtered correctly and, consequently, artifacts from non-existing objects may appear in the output image. Thus, in practice one should always refer to the original 3D images/slices without the threshold. It is also observed that this threshold at some point reduces the size of inclusions in comparison to the reference snapshots in the video. However, if we decrease the threshold, the thin stream adjacent the syringe outlet in the upper layers can become overly thick in the resulting 3D images. Bear in mind the fact that EIT inverse problem is mathematically ill-posed and ill-conditioned. Here we are reconstructing a 32480-pixel 3D image using 208 voltage measurements from 2×16 electrodes. Although the structural *a priori* knowledge is exploited, we can never obtain the exact and true 3D conductivity distribution. Additionally, the injected saline with a conductivity below the EIT sensitivity may still be clearly visible to the naked eyes in the video snapshot due to the bright color of the ink. Thus, the actually conductivity distribution can also disagree considerably with the color dispersion in the vessel.

IV. Conclusion

In summary, for the underlying large-scale inverse problem of 3D EIT reconstruction, this paper has developed an accelerated SA-SBL-based algorithm via AMP, which offers enhanced reconstruction accuracy and reduced artifacts by exploiting 3D structure priors. It is noteworthy that the proposed algorithm is generalizable to other similar process tomography modalities. The advantage of the proposed algorithm over conventional methods has been validated by numerical experiments using real collected measurements, and the visualization of 3D fluid flow process has also been attempted. This study takes an important step towards practical and more sophisticated real-time impedance tomography. The enhanced imaging quality and reduced computational complexity offers exciting possibilities for imaging tasks in several practical applications, such as dispersion control in mixing vessels and monitoring of brain function. Together with its characteristic strength in time and contrast resolution, EIT instrumentation should be able to evolve as an attractive complement/alternative to the prevailing radionuclide modalities in the foreseeable future.

Acknowledgment

The authors would like to acknowledge the insightful input from the anonymous reviewers.

References

[1] M. Marsousi, K. Plataniotis, and S. Stergiopoulos, "Computer-assisted 3-D ultrasound probe placement for emergency healthcare applications," *IEEE Trans. Ind. Inf.*, vol. 12, no. 4, pp. 1380–1391, Aug. 2016.

[2] Y. Motai, D. Ma, and H. Yoshida, "Smart anomaly prediction in nonstationary CT colonography screening," *IEEE Trans. Ind. Inf.*, vol. 12, no. 6, pp. 2292–2301, Dec. 2016.

[3] S. Liu, J. Jia, Y. D. Zhang, and Y. Yang, "Image reconstruction in electrical impedance tomography based on structure-aware sparse Bayesian learning," *IEEE Trans. Med. Imaging*, vol. 37, no. 9, pp. 2090–2102, Sept. 2018.

[4] D. R. Stephenson, J. L. Davidson, and *et al.*, "Comparison of 3D image reconstruction techniques using real electrical impedance measurement data," in *Proc. 4^{th} World Congr. Ind. Process Tomogr.*, Aizu, Japan, pp. 643–650, Sept. 2005.

[5] R. S. Blue, D. Isaacson, and J. C. Newell, "Real-time three-dimensional electrical impedance imaging," *Physiol. Meas.*, vol. 21, no. 1, pp. 15–26, Jan. 2000.

[6] A. P. Calderón, "On an inverse boundary value problem," *Semin. Numer. Anal. Appl. Continuum Phys.*, Rio de Janeiro, Brazil, pp. 65–73, 1980.

[7] A. Wexler, "Electrical impedance imaging in two and three dimensions," *Clin. Phys. Physiol. Meas.*, vol. 9, no. 4A, pp. 29–33, Dec. 1988.

[8] J. Goble, M. Cheney, and D. Isaacson, "Electrical impedance tomography in three dimensions," *Appl. Comput. Electromagn. Soc. J.*, vol. 7, no. 2, pp. 128–147, July 1992.

[9] J. L. Mueller, D. Isaacson, and J. C. Newell, "A reconstruction algorithm for electrical impedance tomography data collected on rectangular electrode arrays," *IEEE Trans. Biomed. Eng.*, vol. 46, no. 11, pp. 1379–1386, Nov. 1999.

[10] A. Le Hyaric and M. K. Pidcock, "An image reconstruction algorithm for three-dimensional electrical impedance tomography," *IEEE Trans. Biomed. Eng.*, vol. 48, no. 2, pp. 230–235, Feb. 2001.

[11] V. Kolehmainen, E. Somersalo, and *et al.*, "A Bayesian approach and total variation priors in 3D electrical impedance tomography," in *Proc. IEEE 20^{th} Annu. Int. Conf. Eng. Med. Biol. Soc. (EMBC)*, Hong Kong, China, pp. 1028–1031, Aug. 1998.

[12] L. Horesh, M. Schweiger, S. R. Arridge, and D. S. Holder, "Large-scale non-linear 3D reconstruction algorithms for electrical impedance tomography of the human head," in *Proc. World Congr. Med. Phys. Biomed. Eng.*, Seoul, Korea, pp. 3862–3865, Aug. 2006.

[13] P. J. Vauhkonen, M. Vauhkonen, T. Savolainen, and J. P. Kaipio, "Three-dimensional electrical impedance tomography based on the complete electrode model," *IEEE Trans. Biomed. Eng.*, vol. 46, no. 9, pp. 1150-1160, Sept. 1999.

[14] E. Somersalo, M. Cheney, and D. Isaacson, "Existence and uniqueness for electrode models for electric current computed tomography," *SIAM J. Appl. Math.*, vol. 52, no. 4, pp. 1023–1040, Aug. 1992.

[15] M. Molinari, S. J. Cox, B. H. Blott, and G. J. Daniell, "Comparison of algorithms for non-linear inverse 3D electrical tomography reconstruction," *Physiol. Meas.*, vol. 23, no. 1, pp. 95–104, Jan. 2002.

[16] N. Polydorides and W. R. B. Lionheart, "A Matlab toolkit for three-dimensional electrical impedance tomography: a contribution to the Electrical Impedance and Diffuse Optical Reconstruction Software project," *Meas. Sci. Technol.*, vol. 13, no. 12, pp. 1871–1883, Dec. 2002.

[17] L. A. M. Mello, C. R. de Lima, and *et al.*, "Three-dimensional electrical impedance tomography: a topology optimization approach," *IEEE Trans. Biomed. Eng.*, vol. 55, no. 2, pp. 531–540, Feb. 2008.

[18] J. Bikowski, K. Knudsen, and J. L. Mueller, "Direct numerical reconstruction of conductivities in three dimensions using scattering transforms," *Inverse Prob.*, vol. 27, no. 1, Art. no. 015002, Jan. 2011.

[19] M. Gehre, T. Kluth, C. Sebu, and P. Maass, "Sparse 3D reconstructions in electrical impedance tomography using real data," *Inverse Prob. Sci. Eng.*, vol. 22, no. 1, pp. 31–44, Jan. 2014.

[20] L. Harhanen, N. Hyvönen, H. Majander, and S. Staboulis, "Edge-enhancing reconstruction algorithm for three-dimensional electrical impedance tomography," *SIAM J. Sci. Comput.*, vol. 37, no. 1, pp. B60–B78, Jan. 2015.

[21] G. González, J. M. J. Huttunen, and *et al.*, "Experimental evaluation of 3D electrical impedance tomography with total variation prior," *Inverse Prob. Sci. Eng.*, vol. 24, no. 8, pp. 1411–1431, Aug. 2016.

TABLE II
3D EIT RECONSTRUCTION RESULTS OF THE JET FLOW.

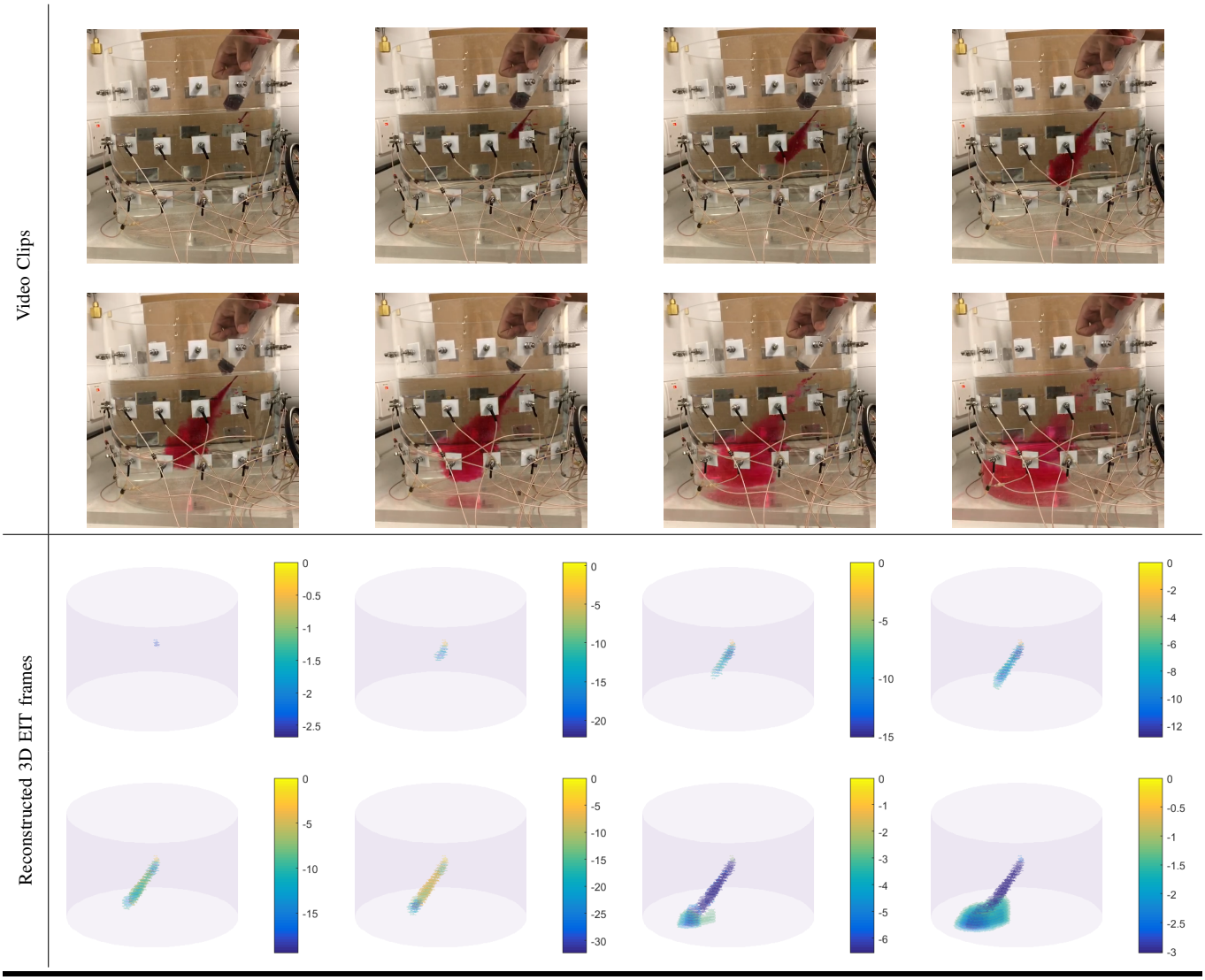

[22] D. Liu, V. Kolehmainen, and *et al.*, "Nonlinear difference imaging approach to three-dimensional electrical impedance tomography in the presence of geometric modeling errors," *IEEE Trans. Biomed. Eng.*, vol. 63, no. 9, pp. 1956–1965, Sept. 2016.

[23] Y. Yang, J. Jia, and *et al.*, "A miniature electrical impedance tomography sensor and 3-D image reconstruction for cell imaging," *IEEE Sens. J.*, vol. 17, no. 2, pp. 514–523, Jan. 2017.

[24] S. N. Das, S. Misra, B. E. Wolfinger, and M. S. Obaidat, "Temporal-correlation-aware dynamic self-management of wireless sensor networks," *IEEE Trans. Ind. Inf.*, vol. 12, no. 6, pp. 2127–2138, Dec. 2016.

[25] X. Gu and S. Wang, "Bayesian Takagi-Sugeno-Kang fuzzy model and its joint learning of structure identification and parameter estimation," *IEEE Trans. Ind. Inf.*, vol. 14, no. 12, pp. 5327–5337, Dec. 2018.

[26] S. Liu, J. Jia, and Y. Yang, "Image reconstruction algorithm for electrical impedance tomography based on block sparse Bayesian learning," in *Proc. 14th IEEE Int. Conf. Imaging Syst. Techni. (IST)*, Beijing, China, pp. 267–271, Oct. 2017.

[27] S. Liu and J. Jia, "Sequential EIT frame reconstruction exploiting spatiotemporal correlation," in *Proc. 19th Int. Conf. Biomed. Appl. Electr. Impedance Tomogr. (EIT)*, Edinburgh, UK, pp. 44, June 2018.

[28] S. Liu and J. Jia, "EIT velocity field estimation via pixel-to-pixel least-squares matching," in *Proc. ISIPT 9th World Congr. Ind. Process Tomogr. (WCIPT)*, Bath, UK, Art. No. P002, Sept. 2018.

[29] M. Bayati and A. Montanari, "The dynamics of message passing on dense graphs, with applications to compressed sensing," *IEEE Trans. Inf. Theory*, vol. 57, no. 2, pp. 764–785, Feb. 2011.

[30] J. P. Vila and P. Schniter, "Expectation-maximization Gaussian-mixture approximate message passing," *IEEE Trans. Signal Process.*, vol. 61, no. 19, pp. 4658–4672, Oct. 2013.

[31] M. Al-Shoukairi, P. Schniter, and B. D. Rao, "A GAMP-based low complexity sparse Bayesian learning algorithm," *IEEE Trans. Signal Process.*, vol. 66, no. 2, pp. 294–308, Jan. 2018.

[32] A. Nissinen, L. M. Heikkinen, and J. P. Kaipio, "The Bayesian approximation error approach for electrical impedance tomography — experimental results," *Meas. Sci. Technol.*, vol. 19, no. 1, pp. 015501, Jan. 2008.

[33] A. Romanowski, "Big data-driven contextual processing methods for electrical capacitance tomography," *IEEE Trans. Ind. Inf.*, in press, (DOI: 10.1109/TII.2018.2855200).

Shengheng Liu (S'14–M'17) received the B.Eng. and Ph.D. degrees in electronics engineering from the School of Information and Electronics, Beijing Institute of Technology, China, in 2010 and 2017, respectively.

Dr. Liu is currently an Associate Professor with the School of Information Science and Engineering, Southeast University, China. Prior to joining SEU, he held a postdoctoral position at the Institute for Digital Communications, The University of Edinburgh, UK, from 2017 to 2018. He also worked as a Visiting Research Associate from 2015 to 2016 at the Department of Electrical and Computer Engineering, Temple University, Philadelphia, PA, USA, under the support of the China Scholarship Council. Dr. Liu is a recipient of the 2017 National Excellent Doctoral Dissertation Award from the China Institute of Communications. His research interests include time-frequency analysis, sparse recovery, statistical learning, electrical tomography, and radar signal processing.

Hancong Wu (S'16) received his B.Eng. (Hons) degrees in electronics and electrical engineering from both The University of Edinburgh, UK, and the South China University of Technology, China, in 2015. He is currently pursuing his Ph.D. degree at the Agile Tomography Group, School of Engineering, University of Edinburgh. His research interests include biosensor, impedance sensing, and electrical impedance tomography for biological applications.

Yongming Huang (M'10–SM'16) received the B.S. and M.S. degrees from Nanjing University, Nanjing, China, in 2000 and 2003, respectively, and the Ph.D. degree in electrical engineering from Southeast University, Nanjing, China, in 2007.

Since 2007, he has been a faculty member with the School of Information Science and Engineering, Southeast University, where he is currently a Full Professor. From 2008 to 2009, he visited the Signal Processing Laboratory, School of Electrical Engineering, Royal Institute of Technology, Stockholm, Sweden. He has authored more than 200 peer-reviewed papers, submitted more than ten technical contributions to the IEEE standards, and hold more than 50 invention patents. His current research interests include MIMO wireless communication, cooperative wireless communication, and millimeter wave wireless communication. He was an Associate Editor for the IEEE TRANSACTIONS ON SIGNAL PROCESSING, IEEE WIRELESS COMMUNICATIONS LETTERS, EURASIP JOURNAL ON ADVANCES IN SIGNAL PROCESSING, and EURASIP JOURNAL ON WIRELESS COMMUNICATIONS AND NETWORKING.

Yunjie Yang (M'13) received his B.Eng. degree from Anhui University, China, in 2010, M.S. from Tsinghua University, China, in 2013, and Ph.D. from The University of Edinburgh, UK, in 2018. From 2013 to 2014, he was a research assistant at the University of Connecticut, Storrs, CT, USA. After obtaining his Ph.D. degree, Dr. Yang was briefly employed as a Postdoctoral Research Associate in Chemical Species Tomography at The University of Edinburgh. He is currently a Chancellor's Fellow in Data Driven Innovation at The University of Edinburgh.

Dr. Yang's research interests are in the areas of sensing and imaging with miscellaneous tomography modalities, and machine learning techniques for process analysis. The goal of his research is to improve the observability in both industrial and biomedical processes, and address the pressing challenges of efficient utilization/interpretation of enormous sensing data. He is the recipient of 2015 IEEE I&M Society Graduate Fellowship Award.

Jiabin Jia (M'15) received the B.Eng. and M.S. degrees in electrical and electronics engineering from the Wuhan University, China, in 2002 and 2005 respectively, and the Ph.D. degree from the University of Leeds supported by the Overseas Research Students Award Scheme in 2010.

He served as a Hardware Engineer at the H3C Technology Co., Ltd in 2006. Following three years working on an EPSRC project as a Research Fellow, he was appointed as a Lecturer at the School of Engineering, The University of Edinburgh in 2013. His current research interests include electrical tomography, acoustic tomography, multiphase flow measurement and medical imaging. He has published more than 30 peer-reviewed journal papers and has contributed to and led a range of research projects.